Available online at www.sciencedirect.com
SCIENCE DIRECT®
Mechanics of Materials 36 (2004) 335–345
MECHANICS OF MATERIALS
www.elsevier.com/locate/mechmat

Failure of silicon nitride under uniaxial compression at high temperature

Massimiliano Gei [a,*], Davide Bigoni [a], Stefano Guicciardi [b]

[a] *Dipartimento di Ingegneria Meccanica e Strutturale, Università di Trento, Via Mesiano 77, I-38050 Trento, Italy*
[b] *IRTEC-CNR, Via Granarolo 64, I-48018 Faenza (RA), Italy*

Received 17 July 2002; received in revised form 2 April 2003

Abstract

Failure modes of silicon nitride cylinders have been investigated under uniaxial compression at 1200 °C in air. Samples with different aspect ratios ($h/d = 5/2$, 4/2, 2/2, and 1/2 mm/mm) have been tested. In all cases, the stress/strain curves evidence an initial linear portion followed by a peak and a slight softening, denoting a plastic behaviour. Surface exfoliation is the dominant failure mode, although traces of localized patterns of deformations—which initiated and propagated macrocracks—can be found in some samples. A bifurcation analysis has been carried out in order to describe the onset of the specific failure mode. The first failure mode predicted by this approach is an antisymmetric mode, while symmetric modes almost immediately follow. However, antisymmetric modes may be partially hampered by friction at the specimen/cushion contact, while symmetric modes could be triggered by residual stress. Therefore, an interpretation of the observed failure mode is that the exfoliation mechanism may result as an evolution of a first antisymmetric mode into a symmetric one and that localized deformations follow to produce final macrocracks growth.

Keywords: Structural ceramics; High temperature; Stress–strain relationship measurements; Plasticity; Bifurcation

1. Introduction

Advanced ceramics are known to be good candidates as materials for high temperature structural applications (Davidge and van de Vorde, 1990; Ichinose, 1987; Larsen et al., 1985; Meetham, 1991; Raj, 1993). Unfortunately, the broad use of ceramic components is restricted by intrinsic limits, like the low fracture toughness, and by a poor knowledge of the mechanical behaviour under the particular conditions in which the material will operate. Being brittle materials, advanced ceramics are mainly tested in tension, as this is considered the most harmful stress condition. However, this does not mean that failure cannot occur when compression loads are involved. From a scientific point of view, failure in compression is an intriguing mechanism, much less investigated than fracture in tension (Ashby and Hallam, 1986; Bazant and Xiang, 1997; Blechman,

* Corresponding author. Tel.: +39-0461-882528/882526; fax: +39-0461-882599.
E-mail addresses: mgei@ing.unitn.it (M. Gei), bigoni@ing.unitn.it (D. Bigoni), guicciardi@irtec.cnr.it (S. Guicciardi).

0167-6636/$ - see front matter © 2003 Elsevier Ltd. All rights reserved.
doi:10.1016/S0167-6636(03)00063-2

1997; Dyskin et al., 1999; Germanovich and Dyskin, 2000; Horii and Nemat-Nasser, 1985; Sammis and Ashby, 1986).

Our interest here is the behaviour of ceramic materials at high temperature and subject to compressive uniaxial stresses. For the specific ceramic under investigation, sintering aids have been used to obtain a fully dense material. These remain as intergranular vitreous phase in the final microstructure of the material. Being less refractory than the ceramic itself, at high temperature this phase becomes viscous promoting viscous flow and grain sliding when stress is applied (Chan and Page, 1993; Lueke et al., 1995; Tsai and Raj, 1982; Wilkinson and Chadwick, 1991). Moreover, due to the high hydrostatic pressure which sets up at the triple grain boundary junctions, cavitation takes place at the intergranular glassy phase, even in compression (Crampon et al., 1997; Lange et al., 1980). At high temperature, when the above-mentioned relaxing mechanisms come into play, both the tensile and the compressive strengths of the material drop. The ratio of the tensile to the compressive strength, which at room temperature is about 1/10 (Atkins and Mai, 1988), increases with temperature and our experiments indicate that the ratio becomes approximately 1/4 at 1200 °C.

A few works on short-term tensile tests appeared in the literature on advanced ceramics at high temperature (Lin et al., 1993; Ohji and Yamauchi, 1994; Ohji et al., 1990; Testu et al., 2001), while little or nothing can be found about short-term compression tests. This study represents an initial contribution in this almost unexplored field. In particular, we observe peculiar modes of failure of our tested cylindrical specimen and we propose an interpretation in terms of bifurcation theory, in which initiation of failure is explained by the occurrence of a surface bifurcation mode.

2. Experimental

The selected material was prepared by mechanically mixing an α-Si_3N_4 powder (S-Stark LC 12 SX, H. C. Stark, New York, NY) with 8 wt.% Y_2O_3 and 3 wt.% Al_2O_3 as sintering aids. The mixture was uniaxially hot-pressed in a graphite crucible under a pressure of 30 MPa at 1810 °C. X-ray diffractometry of the as-sintered material revealed that the main phases were β-Si_3N_4 with $\approx$10% residual α-Si_3N_4. Some relevant microstructural and mechanical properties are summarised in Table 1 (measured at room temperature unless otherwise indicated). Further information can be found in Biasini et al. (1992).

Table 1
Microstructural and mechanical properties of the tested silicon nitride at room temperature

Density (g/cm^3)	3.28
Mean grain size (μm)	0.8
β-grain aspect ratio	$\approx$7
Thermal expansion coefficient (10^{-6} °C^{-1})	3.25
Hardness (GPa)	20.7 ± 0.9
Young modulus (GPa)	301
Toughness (MPa$\sqrt{\text{m}}$)	4.8 ± 0.15
Flexural strength (MPa)	RT 895 ± 35
	1000 °C 603 ± 39
	1300 °C 281 ± 22

From the pellet (45 mm in diameter and 15 mm height), cylinders with a diameter of 2 mm were obtained by machining with their axis parallel to the hot-pressing direction. Samples with different heights were prepared: 1, 2, 4 and 5 mm, respectively. The tests were conducted in air at 1200 °C using an Instron machine mod. 6025 (Instron Ltd., High Wycombe, UK). To avoid excessive friction at the interface, two larger Si_3N_4 cylinders (6 mm in diameter and 3 mm in height) machined from the same billet of the samples were inserted between the sample and the alumina pushrods. All the tests were conducted at a nominal strain rate of 5×10^{-5} s^{-1}. The strain rate was calculated from the specimen height and the crosshead displacement rate. The heating rate was 10 °C/min and, before loading, the sample was allowed to soak for 18 min to insure thermal equilibrium. Most of the tests were stopped after a load drop of about 3–4% of the peak load. The load was removed before the cooling down. Two out of nine samples broke just after the test stop. To observe the full evolution of damage, one thick sample, 1 mm height, was deformed up to 0.12. The sample failure patterns were observed by optical (Leitz DMRME, Leica,

Wetzlar, Germany) and scanning electron microscope (Cambridge Instruments, Cambridge, UK).

3. Results and discussion

Values of the peak loads for the investigated specimens are reported in Fig. 1, with reference to the sample height. The peak load shows a slight tendency to lower when the height of the sample is increased, Fig. 1.

This slenderness effect will be later explained in terms of bifurcation theory and has been also documented for concrete (Hudson et al., 1971). Including all the values reported in Fig. 1, the peak load averages 4509 N with a standard deviation of 303 N. Referring to the flexural strength data reported in Table 1, the ratio of tensile to compressive strength can be estimated to be about 1/4.

A standard procedure may be applied to the load–displacement curves in order to evaluate the effective strain of the sample. The system compliance can be estimated according to the following relationship:

$$C_T = \frac{h}{ES} + C_s, \tag{1}$$

where C_T is the total compliance, h the initial height of the sample, E the Young modulus, S the cross-section of the sample and C_s the system compliance. Using at least three samples with different heights, it is possible to evaluate, by a linear regression analysis, the Young modulus of the material and the system compliance. Subtracting the system compliance from the measured total compliance, the true load–displacement curve of the sample (and whence the nominal stress-deformation behaviour) is obtained. The stress–strain curves calculated in this way are reported in Fig. 2 (six curves are split into Fig. 2(a) and (b) to facilitate reading). The regression analysis gives a Young modulus value of about 105 GPa for 1200 °C.

The general shape of the stress–strain curves does not indicate any significant difference among samples with different height (this is also consistent with results presented by Hudson et al., 1971, for concrete, where the strong difference in the stress/strain curves is observed in the post-peak behaviour, while our experiments—except one—have been interrupted just after the peak).

SEM micrographs of the samples are reported in Figs. 3–6, for different aspect ratios. Figs. 3 and 4 pertain to aspect ratios 2/2 and 1/2, respectively. In both cases a surface exfoliation is evident. The exfoliation layer was quantified to be about 30–35 μm, Fig. 3. Internal cracks can also be observed, Fig. 4. Surface exfoliation is also very clear from Fig. 5 (aspect ratio 4/2). However, this sample was longitudinally sectioned and cracks almost parallel

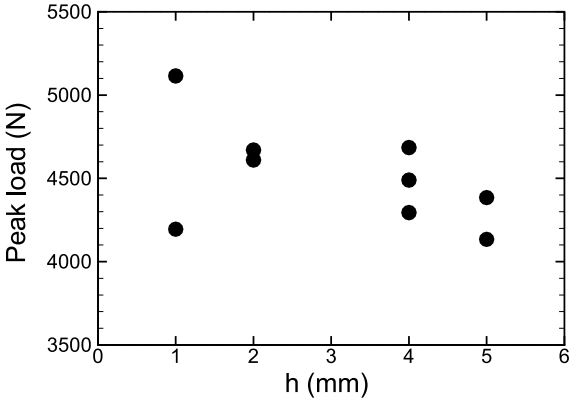

Fig. 1. Compression peak loads vs. sample height (h) for Si_3N_4 cylinders tested at 1200 °C in air.

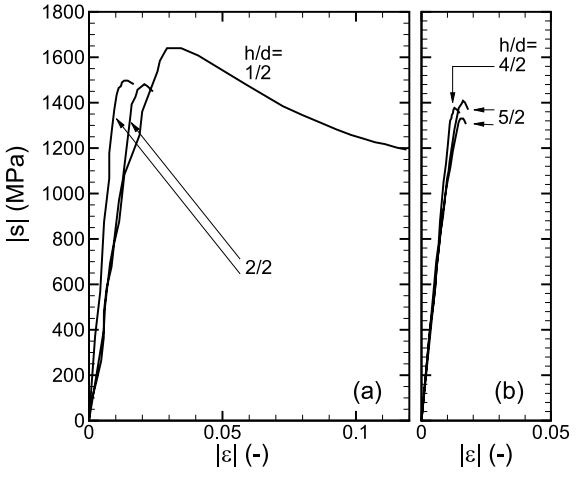

Fig. 2. Compression nominal stress (s)–strain (ε) curves for Si_3N_4 cylinders tested at 1200 °C in air; h/d is the aspect ratio. (a) Data for $h/d = 1/2$, 2/2 and (b) data for $h/d = 4/2$, 5/2.

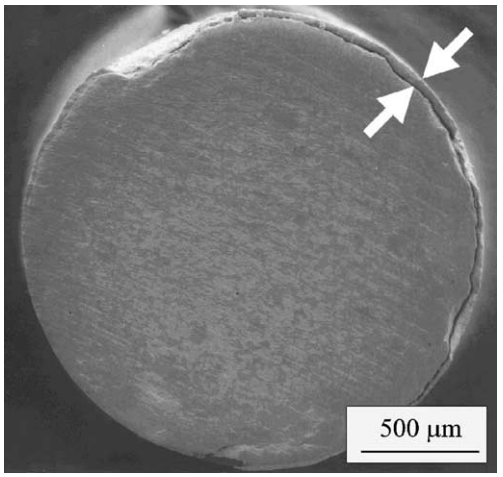

Fig. 3. SEM micrograph of a sample 2 mm height after test. Top view. The arrows indicate the exfoliation layer.

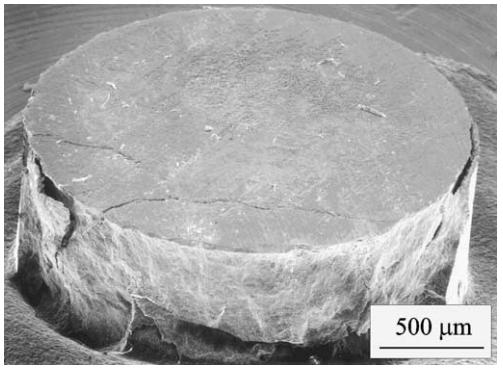

Fig. 4. SEM micrograph of a sample 1 mm height after test.

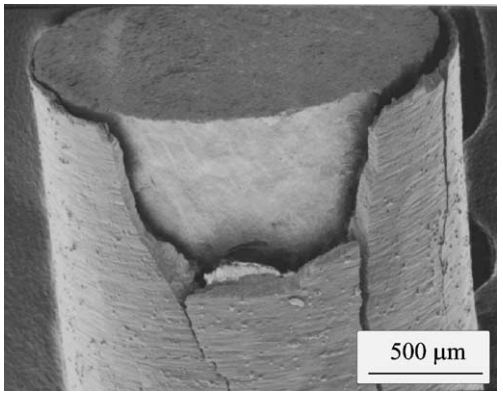

Fig. 5. SEM micrograph of a sample 4 mm height after test.

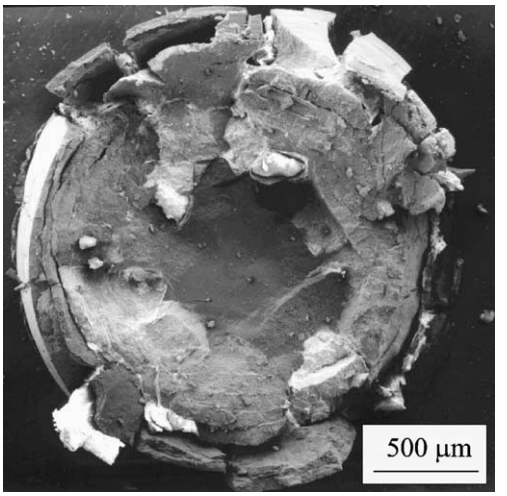

Fig. 6. SEM micrograph of a sample 1 mm height deformed up to 0.12. Top view.

to the loading direction were observed. These may be interpreted as a localized axial-splitting failure mode. The thick sample (aspect ratio 1/2), Figs. 6 and 7, shows once more the surface exfoliation failure mode. Interestingly, this exfoliation is, in this case, a progressive mechanism: at least four exfoliation layers can be detected in Fig. 7 (which gives details of Fig. 6), with almost equal thickness of about 70 μm.

Summarizing, axially-symmetric surface exfoliation is the dominant failure mechanism. This is a mechanism sometimes occurring in rock mechanics (see Fig. 1.2.6 in Vardoulakis and Sulem, 1995) and also found in axial compression of concrete

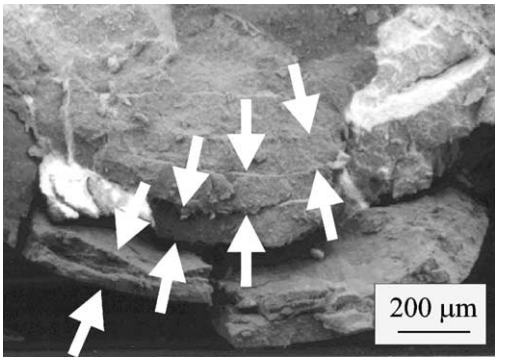

Fig. 7. Detail of micrograph 6. Note the successive exfoliations (indicated through arrows) formed during the test.

(Hudson et al., 1971). The observed failure can be interpreted from a number of perspectives. It can be related to the effect of friction at the specimen/cushion contact, but in our case the test set up was specifically arranged to minimize this effect. Another possibility is to explain failure as an axial splitting phenomenon occurring as consequence of a branching of an inclined crack into a vertical fracture, the so-called "wing-crack growth" (Horii and Nemat-Nasser, 1985). This explanation appears rather weak in our case due to different reasons. First, the crack branching mechanism would generate vertical, nearly-planar cracks (possibly arranged in a macroscopic inclined band; see, for instance, experiments on fresh-water, granular ice, Schulson, 1990), instead of the observed axisymmetric modes. Second, that mechanism is typical of brittle materials, but a ductility is evident in our case, so that behaviour of our material can be classified as "quasi-brittle". Third, the presence of microcracks or defects in the material before the test initiation cannot be a priori excluded in our case, but is very unlikely. Fourth, crack wing growth seems to be a limited phenomenon in three dimensions (see the experimental results on PMMA, Dyskin et al., 1999; Germanovich and Dyskin, 2000).

Alternatively, initiation of failure of our samples can be interpreted as the analogue for, say, a quasi-brittle material of the surface effects observable in metal specimens (Rittel, 1990; Rittel et al., 1991). From this point of view, it may be interpreted as a bifurcation phenomenon: the homogeneous deformation pattern corresponding to the cylindrical shape may cease to be unique and bifurcate into an inhomogeneous pattern with surface undulations, which decay rapidly away from free surface. The problem of bifurcation of a cylindrical specimen subject to uniaxial compression was analyzed by Chau (1992) for rock-like materials and by Bigoni and Gei (2001) for metals. An analysis of these results reveals that the surface mode corresponds usually to bifurcation loads higher than those corresponding to barrelling or antisymmetric modes. Therefore, the explanation of the experimental results needs often to resort to some peculiar physical mechanisms. In rock mechanics, the presence of cracks parallel to the free surface is often invoked for bifurcation to occur (Vardoulakis and Sulem, 1995). For the analyzed material, such type of cracks are first unlikely and, second, they would not produce failure in a axisymmetric fracture mode. On the other hand, due to the fabrication process, a thin layer of material subject to residual stress may exist close to the free surface due to machining. This layer, often detected in ceramic materials (Samuel et al., 1989), could give rise to a surface bifurcation mode occurring before other modes, a situation that can be analyzed in our case using models developed by Bigoni and Gei (2001) and Bigoni et al. (1997). A few, approximate calculations—not reported here for brevity—show however that the residual stress should not play an important role here, except, perhaps, as an imperfection promoting a surface bifurcation mode.

In closure of the present discussion, it may be worth noting that the failure modes observed in our specimens share some similarities with modes relative to the triaxial compression of sand specimens (Desrues et al., 1996). In those specimens, failure has been attributed to a localization of deformation organized in a conical geometry. Although we do not completely agree with that conclusion, [1] strain localization in the sense of Rice (1977) still remains a possibility of explaining our experimental results. To clarify this and the related issue of diffuse bifurcation modes—remaining the most likely explanation for the observed surface exfoliation—we present in the next section explicit calculations of diffuse and localized bifurcations for an elastic model describing the main features of our experimental results.

4. Bifurcation analysis

Testing of materials at high temperature poses such difficulties that a constitutive framework

[1] For fixed top of the testing machine, we think that strain localization should occur along the *two* weaker planes, inevitably present in any real specimen. Therefore, we believe that the localization observed in the sand specimens should have occurred *after* an axisymmetric bifurcation mode has occurred.

should be necessarily built on few experimental data. Therefore, we propose a simple, hyperelastic model taken from the framework of J_2-deformation theory of plasticity (Hutchinson and Tvergaard, 1980; Neale, 1981), to describe our uniaxial experiments. The model is tailored on our experimental results to describe a smooth transition from hardening to softening behaviour in uniaxial compression. Being the description restricted to uniaxial compression we formulate, for simplicity, a model where the behaviour in tension is equal to the behaviour in compression. As a consequence, the model is defined by three material parameters only.

Loss of uniqueness in the incremental response of an incompressible, elastic cylinder subject to uniaxial compression is examined. A bifurcation point is detected when, at a certain stage of the primary path of equilibrium, an inhomogeneous field (called *bifurcation mode*) is found to satisfy the incremental equilibrium equations (in addition to the trivial homogeneous response).

Here, we briefly summarize the equations and the methodology of the bifurcation analysis, referring the interested reader to Bigoni and Gei (2001) for further details.

Let us consider an incompressible cylinder of radius R and height h in the undeformed, natural configuration (C), whose points are labelled by $\boldsymbol{x}$, subject to a homogeneous, axisymmetric deformation $\boldsymbol{\varphi}$. The current configuration $\overline{C} = \boldsymbol{\varphi}(C)$, whose points are denoted by $\bar{\boldsymbol{x}}$, is described by a cylindrical coordinates system (r, θ, z), with z coincident with the axis of the cylinder and origin at its lower base. Let $\{\boldsymbol{e}_r, \boldsymbol{e}_\theta, \boldsymbol{e}_z\}$ be an orthonormal basis associated with the system just introduced.

We adopt the logarithmic strain tensor, $\boldsymbol{\varepsilon}$, as a measure of the strain induced by $\boldsymbol{\varphi}$. In an axisymmetric deformation, the incompressibility constraint, $\det \nabla_C \boldsymbol{\varphi} = 1$, allows to express $\boldsymbol{\varepsilon}$ as

$$\boldsymbol{\varepsilon} = -\varepsilon/2(\boldsymbol{e}_r \otimes \boldsymbol{e}_r + \boldsymbol{e}_\theta \otimes \boldsymbol{e}_\theta) + \varepsilon \boldsymbol{e}_z \otimes \boldsymbol{e}_z, \tag{2}$$

(where $\varepsilon < 0$ in compression) so that the current radius, $\bar{r}$, and height, $\bar{h}$, are given by

$$\bar{r} = \exp(-\varepsilon/2)R \quad \text{and} \quad \bar{h} = \exp(\varepsilon)h, \tag{3}$$

respectively. In the context of small deformations, ε reduces to the axial principal strain. The lateral surface of the cylinder is traction-free and a uniaxial stress is assumed directed along its axis.

In the hyperelastic, finite strain generalization of the J_2-deformation theory the state of the body is fully specified once a strain-energy function is given in terms of effective strain, ε_e, defined as (Hutchinson and Tvergaard, 1980; Neale, 1981)

$$\varepsilon_e = \sqrt{2\boldsymbol{\varepsilon}_{dev} \cdot \boldsymbol{\varepsilon}_{dev}/3}, \tag{4}$$

where $(\cdot)_{dev}$ denotes the deviatoric part of the quantity concerned. In the present situation, the form (2) of $\boldsymbol{\varepsilon}$ leads to

$$\varepsilon_e = |\varepsilon|. \tag{5}$$

The following expression for the strain energy $W(\varepsilon_e)$ is particularly suited to fit the experimental stress–strain curves reported in Fig. 2,

$$W = Kc\varepsilon_0 \left[\frac{1}{c+1}\exp\left(-\frac{\varepsilon_e}{\varepsilon_0}\right) - 1\right]\exp\left(-\frac{\varepsilon_e}{c\varepsilon_0}\right), \tag{6}$$

with $K = 1680$ MPa, $c = 42$, and $\varepsilon_0 = 0.0045$. Indeed, for non-linear, incompressible, isotropic materials undergoing an axisymmetric deformation, the true stress σ aligned along z can be simply derived from the relationship

$$\sigma - \sigma_r = \frac{\partial W}{\partial \varepsilon} = \frac{\mathrm{d}W}{\mathrm{d}\varepsilon_e}\frac{\varepsilon}{\varepsilon_e}, \tag{7}$$

where the lateral stress σ_r vanishes in our case. Therefore, we obtain from (6)

$$\sigma = \frac{K}{\varepsilon_e}\varepsilon\left[1 - \exp\left(-\frac{\varepsilon_e}{\varepsilon_0}\right)\right]\exp\left(-\frac{\varepsilon_e}{c\varepsilon_0}\right), \tag{8}$$

or, in terms of nominal stress s,

$$s = \frac{\sigma}{\exp(\varepsilon)} = \frac{K}{\varepsilon_e}\varepsilon\left[1 - \exp\left(-\frac{\varepsilon_e}{\varepsilon_0}\right)\right]\exp\left(-\frac{\varepsilon_e}{c\varepsilon_0} - \varepsilon\right). \tag{9}$$

The feature of the formulation based on the effective strain ε_e is that for uniaxial stress, the behaviour in compression turns out to be identical to that in tension, a circumstance not fully consistent with our experimental observations, but yielding a substantial simplification in the model.

Consider now an incremental displacement field $\boldsymbol{u}(\bar{\boldsymbol{x}}) = \dot{\bar{\boldsymbol{x}}}$ superimposed upon the current

deformation. In an updated Lagrangian formulation and in absence of body forces, the incremental equilibrium equations may be expressed in terms of increment in the first Piola–Kirchhoff stress tensor, $\dot{\boldsymbol{S}}$, as

$$\mathrm{div}\dot{\boldsymbol{S}} = \boldsymbol{0}. \tag{10}$$

The incremental boundary-value problem is completed by the following boundary conditions:

- null tractions at the lateral surface,

$$\dot{S}_{rr} = \dot{S}_{\theta r} = \dot{S}_{zr} = 0 \quad \text{at } r = \bar{r}, \tag{11}$$

- perfectly smooth contact with a rigid, flat constraint on the faces $z = 0$ and $\bar{h}$,

$$\dot{S}_{\theta z} = \dot{S}_{rz} = u_z = 0 \quad \text{at } z = 0, \bar{h}. \tag{12}$$

The constitutive equations are taken to be linear relationships between $\dot{\boldsymbol{S}}$ and $\boldsymbol{L} = \mathrm{grad}\boldsymbol{u}$ and are expressed, in the specific axisymmetric geometry, in terms of three incremental moduli, μ_i ($i = 1, 2, 3$) (Bigoni and Gei, 2001). In cylindrical components, these are

$$\begin{aligned}
\dot{S}_{rr} &= \dot{p} + 2\mu_2 L_{rr} + 2(\mu_1 - \mu_2)L_{\theta\theta},\\
\dot{S}_{\theta\theta} &= \dot{p} + 2\mu_2 L_{\theta\theta} + 2(\mu_1 - \mu_2)L_{rr},\\
\dot{S}_{zz} &= \dot{p} + (2\mu_1 - \sigma)L_{zz},\\
\dot{S}_{r\theta} &= \dot{S}_{\theta r} = (2\mu_2 - \mu_1)(L_{r\theta} + L_{\theta r}),\\
\dot{S}_{rz} &= \left(\mu_3 + \frac{\sigma}{2}\right)L_{rz} + \left(\mu_3 - \frac{\sigma}{2}\right)L_{zr},\\
\dot{S}_{zr} &= \left(\mu_3 - \frac{\sigma}{2}\right)L_{rz} + \left(\mu_3 - \frac{\sigma}{2}\right)L_{zr},\\
\dot{S}_{\theta z} &= \left(\mu_3 + \frac{\sigma}{2}\right)L_{\theta z} + \left(\mu_3 - \frac{\sigma}{2}\right)L_{z\theta},\\
\dot{S}_{z\theta} &= \left(\mu_3 - \frac{\sigma}{2}\right)L_{\theta z} + \left(\mu_3 - \frac{\sigma}{2}\right)L_{z\theta},
\end{aligned} \tag{13}$$

where $\dot{p}$ is the Lagrange multiplier associated with the incompressibility constraint.

The incremental moduli are functions of the pre-stress, or pre-strain, which affects the incremental response of the solid. In the framework of the hyperelastic, finite-strain generalization of the J_2-deformation theory (Hutchinson and Tvergaard, 1980; Neale, 1981), they can be expressed in terms of $W(\varepsilon_e)$ and of the logarithmic strain, ε, as

$$\begin{aligned}
\mu_1 &= \frac{1}{3}W'', \quad \mu_2 = \frac{1}{6}\left(W'' + \frac{W'}{\varepsilon_e}\right),\\
\mu_3 &= \frac{1}{2}\frac{W'}{\varepsilon_e}\varepsilon\coth\left(\frac{3}{2}\varepsilon\right),
\end{aligned} \tag{14}$$

where a prime denotes differentiation with respect to ε_e.

In order to simplify the formulation, we note that, exploiting the condition of incompressibility of the incremental deformation, namely

$$\mathrm{tr}\boldsymbol{L} = u_{r,r} + (u_r + u_{\theta,\theta})/r + u_{z,z} = 0, \tag{15}$$

the components of $\boldsymbol{u}$ can be written in terms of two displacement potentials, $\Omega = \Omega(r, \theta, z)$ and $\Psi = \Psi(r, \theta, z)$, as

$$\begin{aligned}
u_r &= \Omega_{,rz} + \Psi_{,\theta}/r, \quad u_\theta = \Omega_{,\theta z}/r - \Psi_{,r},\\
u_z &= -\mathscr{M}(\Omega),
\end{aligned} \tag{16}$$

where $\mathscr{M}(\cdot) = (\cdot)_{,rr} + (\cdot)_{,r}/r + (\cdot)_{,\theta\theta}/r^2$ is the two-dimensional Laplacian operator in polar coordinates.

Bifurcations are sought in the separate variables form

$$\begin{cases}
\Omega(r, \theta, z) = \omega(r)\cos n\theta \sin \eta z,\\
\Psi(r, \theta, z) = \psi(r)\sin n\theta \cos \eta z,\\
\dot{p}(r, \theta, z) = q(r)\cos n\theta \cos \eta z,
\end{cases} \tag{17}$$

where $\eta = k\pi/\bar{h}$ ($k = 1, 2, \ldots$) and n ($n = 0, 1, 2, \ldots$) are, respectively, the longitudinal and the circumferential wave numbers. The definition of η assures that boundary conditions (12) are satisfied.

Substitution of Eq. (17) into Eqs. (16), (13), and (10) yields two ordinary differential equations for $\omega(r)$ and $\psi(r)$ and an expression for $q(r)$. The first two equations are

$$\begin{cases}
(\mathscr{L}_n - \rho_3^2\eta^2)\psi = 0,\\
(\mathscr{L}_n + \rho_1^2\eta^2)(\mathscr{L}_n + \rho_2^2\eta^2)\omega = 0,
\end{cases} \tag{18}$$

where $\mathscr{L}_n(\cdot) = d^2(\cdot)/\mathrm{d}r^2 + d(\cdot)/\mathrm{d}r/r - n^2(\cdot)/r^2$ is the Bessel operator, ρ_i^2 ($i = 1, 2$) are the solutions of the characteristic equation

$$(\mu_3 - \sigma/2)\rho^4 + 2(\mu_1 + \mu_2 - \mu_3)\rho^2 + (\mu_3 + \sigma/2) = 0 \tag{19}$$

and

$$\rho_3^2 = (\mu_3 + \sigma/2)/(2\mu_2 - \mu_1). \tag{20}$$

The solutions for $\omega(r)$, $\psi(r)$ and $q(r)$ are

$$\begin{cases} \omega(r) = a_1 J_n(\rho_1 \eta r) + a_2 J_n(\rho_2 \eta r), \\ \psi(r) = b I_n(\rho_3 \eta r), \\ q(r) = (2\mu_1 - \mu_3 - \sigma/2)\eta \mathscr{L}_n(\omega) \\ \qquad -(\mu_3 - \sigma/2)\mathscr{L}_n^2(\omega)/\eta, \end{cases} \tag{21}$$

where a_i $(i = 1, 2)$ and b are arbitrary constants, $J_n(x)$ and $I_n(x)$ are—respectively—the ordinary and the modified Bessel functions of order n.

It is worth noting that the nature of roots $\pm\rho_1$ and $\pm\rho_2$ of Eq. (19) defines the classification of regimes: complex conjugate $\pm\rho_1$ and $\pm\rho_2$ in the elliptic complex regime (EC); pure imaginary $\pm\rho_1$ and $\pm\rho_2$ in the elliptic imaginary regime (EI); real $\pm\rho_1$ and $\pm\rho_2$ in the hyperbolic regime (H); two real and two pure imaginary $\pm\rho_1$ and $\pm\rho_2$ in the parabolic regime (P). It should be noted that failure of ellipticity corresponds to localization of deformation. Therefore, the investigation of bifurcation is restricted to the elliptic range, where $\mu_3 + \sigma/2 > 0$, $2\mu_2 - \mu_1 > 0$, so that the coefficient ρ_3^2, Eq. (20), is always positive either in (EI) or in (EC) regimes.

Eqs. (16)–(21) fully specify the displacement field and, through Eq. (13), the incremental stress state. The imposition of the boundary conditions on the lateral surface, Eq. (11), provides a homogeneous algebraic system for the constants a_i $(i = 1, 2)$ and b. Non-trivial solution are obtained if the determinant of the associated matrix vanishes (*bifurcation condition*). Once the current geometry and state is known, the bifurcation mode has to be selected in terms of the circumferential wave number n and of the dimensionless parameter $\eta\bar{r}$, so that the bifurcation condition determines the critical logarithmic strain ε_{bif}.

4.1. Results

Bifurcation points and modes for samples with aspect ratios 1/2, 2/2, 4/2 and 5/2 have been computed and reported in Figs. 8 and 9. The bifurcation points are marked in Fig. 8 on the uniaxial stress vs. logarithmic strain curves with vertical segments, since they correspond to two different values of Cauchy (or true) and nominal stresses, but to the same value of strain.

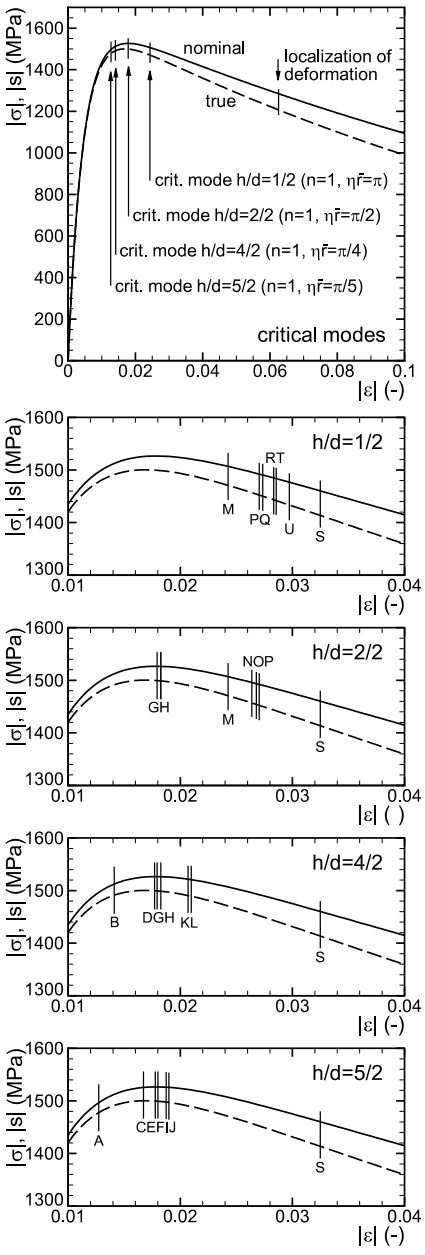

Fig. 8. True (Eq. (8)) and nominal (Eq. (9)) stress vs. logarithmic strain curves (the former is dashed), with superimposed critical points for bifurcation. S denotes surface instability that occurs at $|\varepsilon_{\text{si}}| = 0.0325$. Characteristics of modes A through U are reported in Table 2.

In the present problem, localization of deformation occurs when the (EC)/(H) boundary is

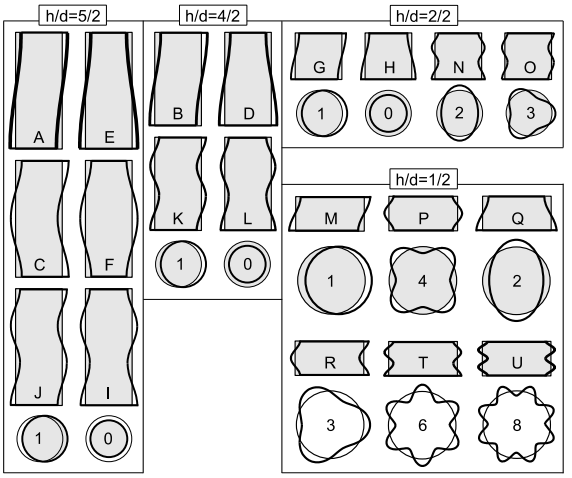

Fig. 9. Sketch of bifurcation modes reported in Fig. 8. Numbers refer to the circumferential wave number n.

touched, i.e. at $|\varepsilon_{\mathrm{loc}}| = 0.0624$, as can be calculated from Eq. (19). The point corresponding to strain localization is reported in the first plot of Fig. 8, where it can be clearly appreciated that *localization always occurs in the strain softening regime*.

The critical, i.e. occurring at lowest strain, bifurcation point for each of the four aspect ratios considered are reported in the first plot of Fig. 8. All the four critical bifurcations correspond to an antisymmetric mode, characterized by $n = 1$. Note that the critical bifurcation occurs

- when the material is still in the hardening regime, for the aspect ratios $h/d = 4/2$ and 5/2,
- at around the peak of stress/strain curve, for the aspect ratio $h/d = 2/2$,
- during softening, for the aspect ratio $h/d = 1/2$.

For aspect ratios higher than 4/2, which would limit possible end-effects, Euler buckling causes premature failure of the specimen, yielding a pronounced size effect.

Bifurcation modes with $n \neq 1$ become available at strains slightly higher than the critical, specially for thick samples. In order to present a complete picture of the bifurcation landscape, the first six modes for every aspect ratio are indicated in Fig. 8 and the relative parameters listed in Table 2. The bifurcation modes are sketched in Fig. 9, where capital letters refer to the classification introduced in Table 2 and numbers denote the values of the circumferential wave number n.

For $h/d = 1/2$ (second plot in Fig. 8), the mode P, following the mode M, is a surface-type mode with double longitudinal wave number—corresponding to half wavelength—and $n = 4$. Moreover, the mode H (axisymmetric) is almost coincident with the mode G (antisymmetric) for the aspect ratio 2/2 (third plot in Fig. 8).

After the sixth mode is attained, infinite bifurcation modes follow one upon other and become closer and closer towards the accumulation point S, representing the surface instability threshold ($|\varepsilon_{\mathrm{si}}| = 0.0325$). Continuing along the uniaxial curve, strain localization occurs as a final instability.

From the reported results it can be clearly understood that *strain localization will never occur in*

Table 2
Bifurcation mode parameters of Fig. 8

Mode	n	$\eta\bar{r}$	$\lvert\varepsilon_{\mathrm{bif}}\rvert$	Mode	n	$\eta\bar{r}$	$\lvert\varepsilon_{\mathrm{bif}}\rvert$
A	1	$\pi/5$	0.0127	K	1	$3\pi/4$	0.0207
B	1	$\pi/4$	0.0141	L	0	$3\pi/4$	0.0208
C	1	$2\pi/5$	0.0167	M	1	π	0.0243
D	0	$\pi/4$	0.0178	N	2	$3\pi/2$	0.0264
E	0	$\pi/5$	0.0178	O	3	$3\pi/2$	0.0268
F	0	$2\pi/5$	0.0179	P	4	2π	0.0270
G	1	$\pi/2$	0.0179	Q	2	π	0.0273
H	0	$\pi/2$	0.0182	R	3	2π	0.0283
I	0	$3\pi/5$	0.0187	T	6	3π	0.0284
J	1	$3\pi/5$	0.0190	U	8	4π	0.0297

a homogeneously deformed specimen, but will take place on a bifurcated deformation path. [2]

We observe that the surface mode S corresponds to an "orange-peel" pattern where both n and $\eta\bar{r}$ diverge. Something similar was found, for a simpler uniaxial stress–strain law than (8), in Bigoni and Gei (2001) for uniaxial tension, but not for compression.

In terms of total compression loads, the nominal peak load calculated from the constitutive law (9) is equal to 4797 N. For $h/d = 4/2$ and 5/2 bifurcation occurs for a load of about 4751 and 4700 N, respectively, indicating the presence of the slenderness effect noticed in the experimental results (Fig. 1). This effect, that is a consequence of loss of uniqueness in the hardening branch, may be observed in specimens having $h/d > 1$.

5. Conclusions

Experimental results have been presented, relative to uniaxial compression at 1200 °C in air of silicon nitride cylinders. Results pertain to different height/diameter ratios. In the experiments, this parameter had only a limited influence on the overall features of the stress–strain curve (which in the present case were interrupted just after the peak) and of the failure modes. For all investigated height/diameter ratios, failure was initiated by surface exfoliation followed by the formation and growth of macrocracks. Three possible interpretations of this behaviour seem to cover all possibilities. These are:

1. Effects related to specimen/cushion friction;
2. Effects related to the presence of microcracks;
3. Effects related to a bifurcation mechanism emerging during deformation.

The first possibility should be minimized with the assumed experimental setup and microcracks can also be excluded, so that the second possibility is also ruled out. Only the last possibility appears relevant to our situation.

In order to investigate the third of the above possibilities, we have proposed an elastic, incompressible model describing our uniaxial experiments and we have performed a complete bifurcation analysis. Results obtained this way may only provide information on the onset of failure, rather than on the development of the exfoliation process. [3] In particular, results show that:

- the first bifurcation mode occurs around the peak of the uniaxial stress/strain curve, in agreement with the observed failure. The fact that bifurcation occurs before for slender than for thick specimens explains the observed slight decrease in the peak load, as related to the increase of the slenderness of the specimen;
- the first possible bifurcation mode is always antisymmetric for all considered geometries;
- the surface modes follow after diffuse mode, but occur "not far" from the first mode;
- localized modes always follow after surface modes.

Following the bifurcation approach, it can be concluded that the observed failure starts at around the peak of the stress–strain curve as an antisymmetric mode [4] and soon degenerates during postcritical behaviour to a surface mode, leading to final failure, with possible strain localization. We believe therefore that bifurcation theory yields a consistent description of the onset of the observed failure modes.

Acknowledgements

M.G. and D.B. gratefully acknowledge financial support of the University of Trento, Italy.

[2] Therefore a calculation of strain localization performed assuming homogeneity may retain some validity only when the bifurcated path followed by the specimen does not involve high strain inhomogeneities.

[3] The exfoliation process implies formation of new boundaries and is therefore a dissipative phenomenon, which cannot be captured within the framework of the present elastic model.

[4] Antisymmetric modes might be at least partially impeded by friction at the specimen/cushion contact, while symmetric surface modes could be promoted by residual stress existing near the external surface.

References

Ashby, M.F., Hallam, S.D., 1986. The failure of brittle solids containing small cracks under compressive stress states. Acta. Metall. 34, 497–510.

Atkins, A.G., Mai, Y.-W., 1988. Elastic and Plastic Fracture. In: Ellis Horwood Series in Engineering Science. Ellis Horwood Ltd, Chichester, UK, p. 175.

Bazant, Z.P., Xiang, Y., 1997. Size effect in compression fracture: splitting crack band propagation. J. Eng. Mech. 123, 162–172.

Biasini, V., Guicciardi, S., Bellosi, A., 1992. Silicon nitride-silicon carbide composite materials. Refract. Metals Hard Mater. 11, 213–221.

Bigoni, D., Gei, M., 2001. Bifurcations of a coated, elastic cylinder. Int. J. Solids Struct. 38, 5117–5148.

Bigoni, D., Ortiz, D., Needleman, A., 1997. Effect of interfacial compliance on bifurcation of a layer bonded to a substrate. Int. J. Solids Struct. 34, 4305–4326.

Blechman, I., 1997. Brittle solid under compression. 1. Gradient mechanism of microcracking. Int. J. Solids Struct. 34, 2563–2581.

Chan, K.S., Page, R.A., 1993. Creep damage development in structural ceramics. J. Am. Ceram. Soc. 76, 803–826.

Chau, K.T., 1992. Non-normality and bifurcation in a compressible pressure-sensitive circular cylinder under axisymmetric tension and compression. Int. J. Solids. Struct. 29, 801–824.

Crampon, J., Duclos, R., Peni, F., Guicciardi, S., de Portu, G., 1997. Compressive creep and creep failure of 8Y(2)O(3)/3Al(2)O(3)-doped hot-pressed silicon nitride. J. Am. Ceram. Soc. 80, 85–91.

Davidge, R.W., van de Vorde, M.H., 1990. Design with Structural Ceramics. Elsevier Science Publishers Ltd, Barking, UK.

Desrues, J., Chambon, R., Mokni, M., Mazerolle, F., 1996. Void ratio evolution inside shear bands in triaxial sand specimens studied by computed tomography. Geotechnique 46, 529–546.

Dyskin, A.V., Germanovich, L.N., Ustinov, K.B., 1999. A 3-D model of wing crack growth and interaction. Eng. Fract. Mech. 63, 81–110.

Germanovich, L.N., Dyskin, A.V., 2000. Fracture mechanisms and instability of openings in compression. Int. J. Rock Mech. Min. Sci. 37, 263–284.

Horii, H., Nemat-Nasser, S., 1985. Compression-induced microcrack growth in brittle solids: axial splitting and shear failure. J. Geophys. Res. 90, 3105–3125.

Hudson, J.A., Brown, E.T., Fairhurst, C., 1971. In: Cording, E.J. (Ed.), Proceedings of the 13th Symposium on Rock Mechanics. University of Illinois Urbana Press, USA.

Hutchinson, J.W., Tvergaard, V., 1980. Surface instabilities on statically strained plastic solids. Int. J. Mech. Sci. 22, 339–354.

Ichinose, N., 1987. Introduction to Fine Ceramics. John Wiley & Sons Ltd, Chichester, UK.

Lange, F.F., Davies, B.I., Clarke, D.R., 1980. Compressive creep of Si_3N_4/MgO alloys. Part. I, effect of composition. J. Mater. Sci. 15, 601–610.

Larsen, D.C., Adams, J.W., Johnson, L.R., Teotia, A.P.S., 1985. Ceramic Material for Advanced Heat Engines. Noyes Publications, Park Ridge, USA.

Lin, C.K.J., Jenkins, M.G., Ferber, M.K., 1993. Tensile dynamic and static fatigue relations for a hiped silicon-nitride at elevated temperatures. J. Eur. Ceram. Soc. 12, 3–13.

Lueke, W.E., Wiederhom, S.M., Hockey, B.J., Long, G.G., Krause Jr., R.F., 1995. Cavitation contributes substantially to creep in silicon nitride. J. Am. Ceram. Soc. 78, 2085–2096.

Meetham, G.W., 1991. High-temperature materials—A general review. J. Mater. Sci. 26, 853–860.

Neale, K.W., 1981. Phenomenological constitutive laws in finite plasticity. In: SM Archives, vol. 6. Sijthoff and Noordhoff International Publishers, Alphen aan den Rijn, The Netherlands.

Ohji, T., Yamauchi, Y., 1994. Diffusional crack growth and creep rupture of silicon carbide doped with alumina. J. Am. Ceram. Soc. 77, 678–682.

Ohji, T., Yamauchi, Y., Kanematsu, W., Ito, S., 1990. Dependence of high-temperature tensile strength on displacement rate for hot-pressed silicon-nitride. J. Mater. Sci. 25, 2990–2996.

Raj, R., 1993. Fundamental research in structural ceramics for service near 2000 degrees C. J. Am. Ceram. Soc. 76, 2147.

Rice, J.R., 1977. The localization of plastic deformation. In: Koiter, W.T. (Ed.), Theoretical and Applied Mechanics. North-Holland, Amsterdam, pp. 207–220.

Rittel, D., 1990. The influence of microstructure on the macroscopic patterns of surface instabilities in metals. Scripta Metall. Mater. 24, 1759–1764.

Rittel, D., Aharonov, R., Feigin, G., Roman, I., 1991. Experimental investigation of surface instabilities in cylindrical tensile metallic specimens. Acta. Metall. Mater. 39, 719–724.

Sammis, C.G., Ashby, M.F., 1986. The failure of brittle porous solids under compressive stress states. Acta. Metall. 34, 511–526.

Samuel, R., Chandrasekar, S., Farris, T.N., Licht, R.H., 1989. Effect of residual stresses on the fracture of ground ceramics. J. Am. Ceram. Soc. 72, 1960–1966.

Schulson, E.M., 1990. The brittle compressive fracture of ice. Acta. Metall. Mater. 38, 1963–1976.

Testu, S., Rouxel, T., Besson, J.-L., 2001. Tensile behaviour of gas pressure sintered silicon nitride in the 1600–1700 °C temperature range. Acta. Mater. 49, 3589–3596.

Tsai, R.L., Raj, R., 1982. Acta. Metall. 30, 1043.

Vardoulakis, I., Sulem, J., 1995. Bifurcation Analysis in Geomechanics. Chapman & Hall, London, UK.

Wilkinson, D.S., Chadwick, M.M., 1991. Creep mechanisms in glass-containing ceramics. J. Phys. III 1, 1131–1139.